Characterization of the Solid–Electrolyte Interphase Growth During Cell Formation Based on Differential Voltage Analysis

Felix Schomburg, Robin Drees, Michael Kurrat, Michael A. Danzer, and Fridolin Röder*

The solid–electrolyte interphase (SEI) in lithium-ion batteries is mainly built during cell formation. The SEI significantly influences safety, aging, and performance. Due to the manifold influential factors, it is time-consuming to systematically optimize the cell formation. Herein, a novel procedure to characterize the SEI growth during the first cycle of formation with low experimental effort is introduced. Coin cells in a three-electrode setup are tested under pseudo-open-circuit conditions. By evaluating the differential voltage, the capacity loss due to SEI formation during the first cycle is estimated. The identification of the SEI growth curve is carried out using various methods, which are compared in detail. The approach is exemplary applied to compare different electrolytes. It is shown that the approach can be used to parameterize SEI growth models. An analysis of these models indicates that the SEI growth can be explained by a combination of two growth mechanisms, that is, interstitial diffusion and electron tunneling, while the latter is dominant in the beginning of the formation. Further, based on the results it is suggested that the transition between these mechanisms is influenced by the electrolyte.

F. Schomburg, M. A. Danzer, F. Röder
Bavarian Center for Battery Technology (BayBatt)
University of Bayreuth
95448 Bayreuth, Germany
E-mail: fridolin.roeder@uni-bayreuth.de

R. Drees, M. Kurrat
elenia Institute for High Voltage Technology and Power Systems
Technische Universität Braunschweig
38106 Braunschweig, Germany

R. Drees, M. Kurrat
Battery LabFactory Braunschweig
Technische Universität Braunschweig
38106 Braunschweig, Germany

M. A. Danzer
Chair of Electrical Energy Systems
University of Bayreuth
95447 Bayreuth, Germany

The ORCID identification number(s) for the author(s) of this article can be found under https://doi.org/10.1002/ente.202200688.

1. Introduction

The solid–electrolyte interphase (SEI) is mainly built during the first charge/discharge cycles of a lithium-ion battery (LIB), the so-called cell formation. The SEI consists of electrolyte decomposition products, which deposit on the surface of the particles at the negative electrode. This layer prevents further reduction reactions of the electrolyte. The properties of the SEI are crucial for aging behavior,[1–4] rate capability,[5,6] and safety.[1,3,7] The composition and morphology of the SEI are influenced by many factors, such as electrolyte composition,[8–10] anode material composition,[11,12] electrode structure,[13] temperature,[14–16] and the applied formation protocol.[17–19] Understanding these manifold influencing factors and establishing predictive models are important to optimize the cell formation process.

To build a growth model for cell formation, the growth-limiting mechanisms need to be identified. Several limiting processes for the SEI growth are under debate and may also vary for different electrolytes, because it influences the SEI composition[20] and each compound has distinct transport properties.[21,22] Electron conduction,[23,24] electron tunneling (ET),[25,26] diffusion of lithium via an interstitial "knock-off" mechanism[21,27] through the SEI, and diffusion of solvent/salts in the bulk[28,29] are the most prominent mechanisms that have been proposed. For the identification and validation of growth models, experimental characterization of the SEI and its thickness evolution during formation is needed.

There are already a large number of experimental and simulation studies on the SEI film growth. Many experimental methods have been used to study the effects of formation on the SEI. Lu et al.[30] conducted a comprehensive study using electrochemical impedance spectroscopy (EIS), X-Ray photoelectron spectroscopy (XPS), time-of-flight secondary-ion mass spectrometry, and scanning electron microscopy (SEM) measurements. Combining their experimental insights, they come to the conclusion that early in the formation process, at high anode potentials, low conductive organic species are loosely deposited on the particle surface. Later, at lower anode potentials, inorganic components with a higher conductivity are formed. Leroy et al.[31] analyzed the SEI using XPS and atomic force microscope (AFM) at different potentials of the first and the fifth cycle.

Their results show that SEI formation occurs in successive sections, which depend on the potential of the negative electrode, and they observed a partial dissolution and redeposition of SEI components. Hou et al.[26] observed such a bilayer structure using mass-sensitive scanning transmission electron microscopy (TEM) and a Li–Au model system. They suggest that the inorganic and organic layers grow in parallel and that this process is driven by ET in the beginning. After reaching a certain thickness, the subsequent growth is assisted by radicals that may originate from the initial formation or diffuse from the bulk to the electrolyte solution. Tang et al.[25] used EIS measurements to investigate the SEI formation on glassy carbon under potentiostatic conditions and deduced time-dependent capacity loss curves at different potentials. They conclude that the limiting process may differ for other electrode structures and formation protocols. Witt et al.[32] applied a physicochemical model in combination with EIS and C-rate tests to obtain interphase and bulk properties of the SEI layer after the formation as well as during battery aging. They conclude that a thicker SEI does not necessarily yield a significant impedance rise.

The SEI thickness has also been directly measured using in situ spectroscopic ellipsometry,[33] TEM,[34] sputter depth profiling, and XPS[35] or photoelectron spectroscopy and soft XPS.[36] Moreover, a combination of focused ion beam, SEM, and XPS was applied to measure the layer thickness.[37] The disadvantage of these methods is that the experimental setup is often complicated, because the SEI is unstable and sensitive to air. As a consequence, it is difficult to investigate a large parameter space with the currently available experimental methods. This hinders to understand the growth limiting mechanisms during formation.

In addition to the experiments, various modeling methods have been used to simulate the SEI formation. As the film growth is influenced at multiple lengths and time scales, simulations are carried out at multiple scales. Lithium-ion transport through SEI has been investigated with molecular dynamics (MD).[21,38] Density functional theory (DFT) simulations were used to investigate the transport processes within the SEI[27,39,40] as well as the reduction reaction in electrolyte solutions.[41,42] Lin et al.[39] performed DFT simulations and suggested that ET is responsible for the initial capacity loss during formation. The tunneling barrier was found to be $2 - 3\,nm$ for inorganic species, i.e., LiF, Li_3PO_4, and Li_2CO_3, and to alter under tension/compression. Kinetic Monte Carlo simulations were applied to study the heterogeneity of the layer[43] and coupled with cell models to account for multiscale effects of the surface film growth.[44,45] The SEI has been studied with continuum models to depict the film thickness and resistance as well as to study the transport processes.[22,46,47] The model proposed by Christensen et al.[47] included the transport of lithium and electrons through the film to simulate the SEI growth. Colclasure et al.[48] implemented a single-particle model that incorporates reaction kinetics and transport of species within the SEI film and was used to study the layer growth and resistance under cycling conditions.

Despite the many experimental and simulative investigations, the knowledge about the build-up during the first cycle of the formation and the involved transport mechanism is still limited due to its complexity and the required experimental effort. Accordingly, novel methods, which are ideally capable to quickly obtain operando information about the SEI thickness, are needed.

In this work, we present a novel approach to determine SEI thickness during the first cycle of the formation, which enables to identify growth models. The method uses coulomb counting and differential voltage analysis (DVA) to gain an operando estimate of an effective SEI thickness during the first charge/discharge. DVA is an established method to differentiate between aging phenomena.[49–51] It also has been applied to study long-term SEI growth.[52] However, to our best knowledge, DVA has not been applied to study capacity loss and SEI growth already during the formation. To facilitate the estimation of the effective SEI thickness using DVA, we propose three methods that evaluate the difference between a reference pseudoopen-circuit potential (pOCP) and the potential during formation: 1) single-characteristic points, 2) identification of the effective SEI thickness as a time series without restrictions, and 3) direct identification of SEI growth models. The methods are compared and discussed in terms of their advantages and disadvantages. As an application example, the influence of two electrolytes on the SEI growth is analyzed.

2. Experimental Section

Coin cells in the three-electrode setup (PAT-Cells from EL-Cell GmbH, Hamburg) were used for electrochemical experiments. Alternatively, also half cells with a lithium counter electrode could be used. Two different electrolyte types and two different electrode sheets of the negative were used. Different electrode sheets were used to account for fluctuations of the mass loading in between manufacturing batches. The specific surface area of the anode and cathode material batches was determined by Brunauer–Emmett–Teller measurements. The nominal and measured properties of the cell components, that is, electrode, electrolyte, and separator, are given in Table S1, Supporting Information.

The cells were assembled in an argon glovebox (M. Braun LABstar/MB10, Garching) with less or equal to 0.5 ppm H_2O and O_2. All experimental cell tests were conducted with a battery test system (PAT-Tester-x-8 from EL-Cell GmbH, Hamburg) in a climate chamber (WT11-600/40 from Weiss Technik GmbH, Reiskirchen) at 20 °C. After cell assembly, the cells were stored in the 20 °C climate chamber for at least 7 h to provide homogeneous electrolyte wetting.

In total, six cells were tested with the same test protocol. The protocol is illustrated in **Figure 1** and includes four parts, i.e., formation, end-of-line (EOL) test, capacity test, and open-circuit-voltage test (OCV test). Only the first charge and discharge
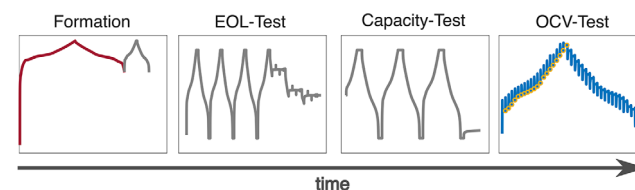

Figure 1. Illustration of the test protocol. Measurements needed to conduct the DVA are highlighted and include the first charge and discharge cycle of the formation being plotted in red, the continuous OCV measurement being plotted in blue, and the OCV sample points being plotted with yellow markers.

(solid red line) and the OCV test (yellow marks) were used in this work. The six cells could be classified into three groups with two cells each: Group A1 with electrolyte A and sheet 1 (cell 1–2), group A2 with electrolyte A and sheet 2 (cell 3–4), and group B2 with electrolyte B and sheet 2 (cell 5–6).

The theoretical capacity was calculated based on the cell configuration and was given as $180 \, \text{mAh} \, \text{g}_{\text{NMC}}^{-1}$. It was used to set the current rate of the formation. After wetting, the first cycle of the formation cycle was started with a current of C/20 until 4.2 V followed by C/20 discharge until 3.0 V. The second formation cycle had a current of C/2 until 4.2 V with CV until I < C/20, followed by C/2 discharge until 3.0 V. The nominal capacity after the formation was determined by a C/3 discharge and equaled $150.32 \pm 0.29 \, \text{mAh} \, \text{g}_{\text{NMC}}^{-1}$ for cells of group A2 and $150.17 \pm 0.43 \, \text{mAh} \, \text{g}_{\text{NMC}}^{-1}$ for group B2.

The OCV test was carried out with 5% state of charge (SOC) steps. The SOC was based on the nominal capacity after formation. The cells were (dis-)charged with 0.5 C for an SOC $\leq 80\%$. At higher SOCs, 0.25 C was used. The cell was relaxed for 2 h after each SOC step before the voltage value was taken.

Besides the protocol for testing the cells, an additional electrochemical experiment with electrolyte A was performed. This cell was assembled using sheet 1 for the negative electrode and a thicker positive electrode (theoretical areal capacity $4.62 \, \text{mAh} \, \text{cm}^{-2}$), which was $\approx 12\%$ overbalanced in comparison with the anode. A thicker positive electrode was used to obtain the full-reference potential range of the negative electrode. The formation procedure of this additional test was a C/20 charge until the potential of the negative electrode, Φ_{ne}, reached 0.01 V. Afterward, there were 11 cycles of discharging/charging with C/20 between 0.5 and 0.01 V of the anode potential, Φ_{ne}, to ensure that a stable SEI was established. Finally, the cell was completely discharged until 3.0 V of Φ_{ne}. The last charge and discharge were used to determine the reference pOCP curve.

3. Methods for DVA-Based Characterization of Formation

DVA is an established technique to separate and quantify aging mechanisms. Therefore, the electrical potential of half or full cells is used. Usually, the cell is tested under quasiequilibrium conditions. This means a low current, which is typically $\leq 1/20$ of the theoretical cell capacity, $C_{\text{theo}}^{\text{Ah}}$, is applied to obtain a continuous potential curve while keeping the electrode polarization negligible. Depending on whether half- or full-cell aging aspects are being investigated, the negative and positive electrode-specific potential profiles versus a lithium metal reference, the full-cell voltage, or a combination are used. Derivatives of the voltage signals with respect to the (dis-)charge capacity are computed. The resulting curves show distinctive maxima and minima, that is, features, which shift as the electrode ages. In aging studies, the method allows to differentiate between loss of active material and loss of lithium inventory. Therefore, the positions of the peaks during aging are compared with their positions after formation, which is usually referred to as the initial state or beginning of life. This approach was applied in many aging studies. The influence of electrolyte additives on a capacity fade in calendaric and cycle life was investigated by Bloom et al.[53] Their analysis of the full- and half-cell data indicates that the decline in available lithium is mainly due to side reactions occurring at the negative electrode and is influenced by the additive. Keil et al.[50] investigated the capacity fade during calendaric aging and showed that the decline in capacity primarily results from losses of cyclable lithium due to continued SEI growth. Moreover, it was found that the capacity fade correlates with the potential of the negative electrode. Furthermore, the DVA was used by Fath et al.[54] to investigate the homogeneity of lithium distribution inside the cell as well as to parameterize predictive lifetime models using automotive pouch cells. A tool to analyze changes in the active masses and slippage of lithium content for each electrode during cell aging was developed by Dahn et al.[55] Müller et al.[56] applied the DVA after the formation process was completed to study the importance of a CV step during formation on aging behavior. They noticed that omitting the CV charging step leads to a worsened degradation behavior of the anode and results in an accelerated loss of cycleable lithium, which they attribute to an unfavorable SEI formation.

The utilization of the DVA in aging studies differs from its utilization in this work. As the scope of this study is the SEI growth during cell formation, the negative electrode potential during the first cycle of the formation, that is, before the beginning of life, is investigated. To gain information about the SEI growth during cell formation, coulomb counting and DVA are combined. The method includes evaluation of the differential voltage during formation and differential voltage after formation, which is used as a reference. The characterization involves several preparation steps that are described in Section 3.1. Afterward, three possible methods to deduce the SEI capacity loss during formation are described in Section 3.2. Finally, the assumptions implied in this identification procedure are summarized in Section 3.3.

3.1. Cell Individual Determination of the SEI Thickness

In this section, the required steps to determine the cell individual SEI thickness from the formation data and a reference measurement by applying DVA and coulomb counting are described. Therefore, the reference potential curve is introduced in Section 3.1.1. In Section 3.1.2, the procedure for determining cell individual capacity and surface area is outlined. Afterward, in Section 3.1.3, it is described how the capacity loss due to the SEI growth during the first cycle of the formation is derived. Finally, the conversion of the SEI capacity into an effective layer thickness is shown in Section 3.1.4.

3.1.1. Determination of the Reference Potential

The material-dependent potential profile of the negative electrode was measured with pseudo-open-circuit conditions in an additional experiment, as described in Section 2. The degree of lithiation (DoL), x_{DoL}, is defined as the ratio between the amount of lithium ions, that is, charge being intercalated, Q_{int}, into the host electrode and the electrode capacity, $C_{\text{electrode}}^{\text{Ah}}$, which can be written as

**ADVANCED
SCIENCE NEWS**

www.advancedsciencenews.com

Energy Technology
Generation, Conversion, Storage, Distribution

www.entechnol.de

$$x_{\mathrm{DoL}} = \frac{Q_{\mathrm{int}}}{C_{\mathrm{electrode}}^{\mathrm{Ah}}} \tag{1}$$

The reference measurement shows a coulombic efficiency of >99.5%, which enables to measure intercalated charge by integrating the measured current $Q_{\mathrm{int}}(t) \approx \int I(t)\,\mathrm{d}t$. With this, the potential of the negative electrode for lithiation and delithiation is determined as a function of the DoL for charge

$$\Phi_{\mathrm{ne,ref}}^{\mathrm{ch}} = f_{\mathrm{ne,ref}}^{\mathrm{ch}}(x_{\mathrm{DoL}}) \tag{2}$$

and discharge

$$\Phi_{\mathrm{ne,ref}}^{\mathrm{dch}} = f_{\mathrm{ne,ref}}^{\mathrm{dch}}(x_{\mathrm{DoL}}) \tag{3}$$

Both functions are shown in **Figure 2**a. Here, the typical characteristic features of the potential of the graphite electrode and the potential hysteresis can be seen. The position of the curve has been manually adjusted by means of the stages shown by Heß et al.[57] (Figure S1, Supporting Information).

Figure 2b shows the derivative of the negative electrode potential with respect to the DoL. Within the derived potential curve distinctive peaks can be seen, some originate from the transition between the characteristic graphite intercalation stages. One characteristic feature, γ, is indicated as an example. Further distinctive features can also be identified in the second derivative of the potential curve. Each feature, γ, can be assigned to a particular DoL, $x_{\mathrm{DoL},\gamma}$.

3.1.2. Determination of the Individual Capacities and Surface Area

To investigate the SEI thickness during formation, the actual capacity and surface area of the negative electrode are determined for every individual cell. The cell individual absolute surface area of the negative electrode, A_{ne}, is calculated as
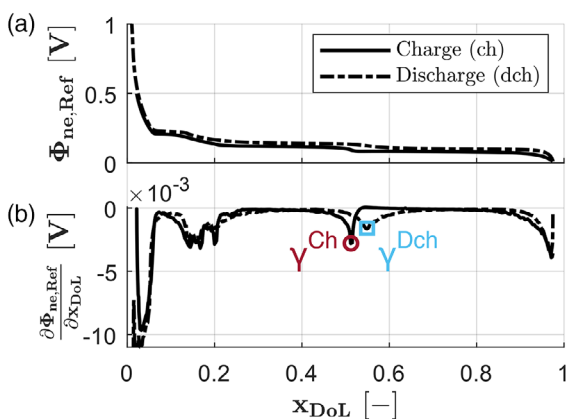

Figure 2. a) Reference potential of the negative electrode versus Li against DoL, obtained under pseudoopen-circuit conditions and its b) first derivative. The charge direction is plotted as a solid line (lithiation of the electrode). Discharge direction is depicted as a dashed/dotted line (delithiation of the electrode). In addition, an example feature in each charging direction is marked with a red circle (charge) and a blue square (discharge).

$$A_{\mathrm{ne}} = \frac{C_{\mathrm{ne}}^{\mathrm{Ah}}}{\mathrm{F}\,c_{\mathrm{max,ne}}}\,a_{\mathrm{s,ne}} \tag{4}$$

with $C_{\mathrm{ne}}^{\mathrm{Ah}}$ being the cell individual capacity of the negative electrode, $a_{\mathrm{s,ne}}$ being the specific surface area of the negative electrode active material, F being Faraday's constant, and $c_{\mathrm{max,ne}}$ being the theoretical maximum concentration of the negative electrode, which is determined based on the structural formula of fully lithiated graphite $\mathrm{LiC_6}$ and its bulk density being $27848\,\mathrm{mol\,m^{-3}}$. The specific surface area $a_{\mathrm{s,ne}}$ is obtained from the measured surface area per weight (Table S1, Supporting Information) with the nominal graphite density ($\rho_{\mathrm{C_6}} = 2.2 \times 10^6\,\mathrm{g\,m^{-3}}$).

The determination of cell individual capacity of the negative electrode is assessed similar to the approach used by Dahn et al.[55] To estimate the capacity, the differential voltage of the reference is compared with the differential curve of every individual cell (cell 1–6) using the OCV test measurement in charge direction. The used OCV sample points are indicated in Figure 1. The OCV sample points are interpolated. Generally, the electrode capacity can then be determined as

$$C_{\mathrm{ne}}^{\mathrm{Ah}} = \frac{Q_{\gamma_{\mathrm{k}}}^0 - Q_{\gamma_{\mathrm{s}}}^0}{x_{\mathrm{DoL},\gamma_{\mathrm{k}}} - x_{\mathrm{DoL},\gamma_{\mathrm{s}}}} \tag{5}$$

using the charge throughput, Q^0, which is determined by coulomb counting, that is, current integration

$$Q_{\gamma}^0 = \int_{t=0}^{t_{\gamma}} I(t)\,\mathrm{d}t \tag{6}$$

from $t = 0$, that is, fresh cell before formation, until the feature, γ. Features γ_{k} and γ_{s} are two distinct features that are identified in the reference and the cell individual OCV test. $x_{\mathrm{DoL},\gamma_{\mathrm{k}}}$ and $x_{\mathrm{DoL},\gamma_{\mathrm{s}}}$ is the corresponding DoL of the reference. Practically, three features were used to reduce the uncertainty of the capacity estimation. The obtained electrode capacities of each cell are listed in Table S2, Supporting Information. The OCV curves, after the determination of electrode capacities, together with the pOCV reference, are shown as a function of the DoL in Figure S2, Supporting Information.

3.1.3. Determination of the Capacity Loss Due to SEI Growth

Based on the cell individual electrode capacity, the capacity loss can be calculated for every identified feature as

$$Q_{\mathrm{loss},\gamma} = Q_{\gamma}^0 - C_{\mathrm{ne}}^{\mathrm{Ah}}\,x_{\mathrm{DoL},\gamma} \tag{7}$$

with $Q_{\mathrm{loss},\gamma}$ being the capacity loss at the negative electrode at the point in time, t_{γ}, when feature γ appears. This capacity loss, in case other degradation processes are negligible, can be assigned to the loss due to SEI side reactions, which yields

$$Q_{\mathrm{SEI},\gamma} \approx Q_{\mathrm{loss},\gamma} \tag{8}$$

being the capacity of the SEI at t_{γ}.

The estimation of the SEI capacity during formation with this approach is illustrated in **Figure 3**. In Figure 3a, the potential of

**ADVANCED
SCIENCE NEWS**

www.advancedsciencenews.com

Energy Technology
Generation, Conversion, Storage, Distribution
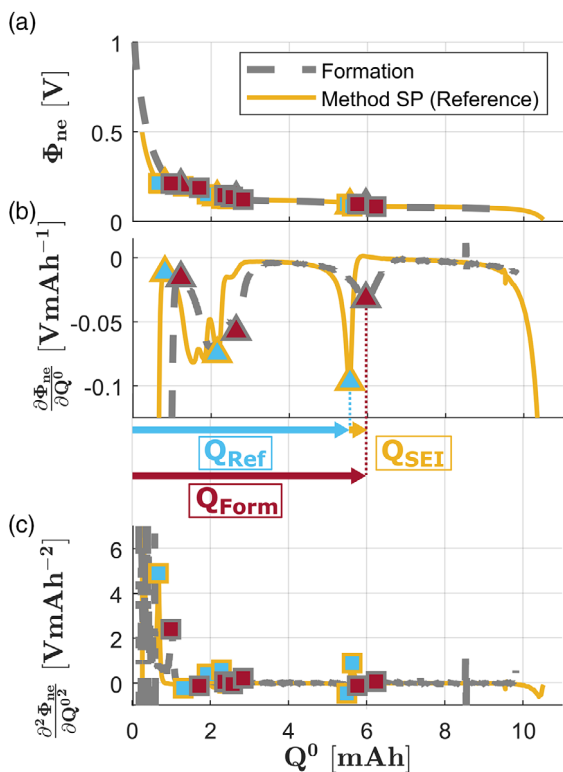
www.entechnol.de

Figure 3. a) Potential of the negative electrode versus the charge throughput for the formation measurement (dashed gray) and the reference (solid yellow). b) First derivative of electrode potential, $\partial\Phi_{ne}/\partial Q^0$, versus the charge throughput. The capacity loss due to SEI formation Q_{SEI} between two example points with equal DoL is indicated with a yellow arrow. Red and blue arrows indicate the charge throughput for an example feature for the formation and the reference, respectively. c) Second derivative of the electrode potential, $\partial^2\Phi_{ne}/\partial(Q^0)^2$, versus the charge throughput. Characteristic points identified using the first and the second derivative are marked with triangles and squares, respectively. Markers filled with blue are depicted with the reference and markers filled with red are depicted with the formation.

the negative electrode (solid yellow line) is shown for the formation during the first charging cycle against the charge throughput, Q^0. If no side reactions occur, the according potential during charge can be estimated using the reference potential as

$$\Phi_{ne,ref}^{ch}(Q^0) = f_{ne,ref}^{ch}\left(\frac{Q^0}{C_{ne}^{Ah}}\right) \tag{9}$$

In Figure 3b, the first derivative of the potential is shown for the formation (gray dashed line) and the reference (solid yellow line). It can be seen that both curves have similar features, which presumably correspond to the same DoL. The difference in total accumulated capacity at equal features can be assigned to SEI capacity, as given by Equation (7) and (8). Any feature of the anode potential during formation, that can be distinctly identified in both potential curves can be used to estimate the capacity loss due to SEI growth. Using the time, t_γ, when a feature appears in the formation, the capacity loss due to SEI growth can be given as a function of time.

$$Q_{SEI}(t_\gamma) = Q_{SEI,\gamma} \tag{10}$$

There are various possible approaches on how to make an assignment between reference and formation measurement. Some possible approaches are applied in this work and are introduced in Section 3.2.1–3.2.3.

3.1.4. Calculation of SEI Thickness from Capacity Loss

The capacity loss due to SEI growth is converted into an effective layer thickness. The effective layer thickness depicts the complex properties of the layer as a simplified dense layer. Due to this simplification, morphological aspects are neglected and it is assumed that the SEI forms as a solid layer on top of the surface area of the negative electrode. Based on these assumptions, the volume of the SEI, V_{SEI}, can be calculated as

$$V_{SEI}(t) = \frac{Q_{SEI}(t)}{2\,F}\frac{M_{SEI}}{\rho_{SEI}} \tag{11}$$

with M_{SEI} being the molar mass and ρ_{SEI} being the density of the effective SEI. As an approximation, the material properties of Li_2CO_3 are used, because it was reported to be a major SEI component in the near-particle region.[31,58,59] This approximation is frequently used for SEI growth simulations.[47,48,60]

Further, the SEI thickness depends on the total surface area.[13] Using the cell individual absolute electrode surface area from Equation (4), the effective SEI thickness can be calculated as

$$L_{SEI}(t) = \frac{V_{SEI}(t)}{A_{ne}} \tag{12}$$

3.2. Methods to Deduce the SEI Capacity

In this section, three possible methods to deduce the SEI capacity during the first cycle of the formation are outlined. First, the determination of the SEI capacity based on single-characteristic points is described. Second, an optimization procedure for determining the SEI capacity using a time series is presented. Third, a method that applies SEI growth models is presented.

3.2.1. Single-Characteristic Point-Based Method

By evaluation of single-characteristic points, that is, feature γ, of the differential voltage, the formation capacity loss and SEI thickness at these points can be estimated. This approach will be referred to as SP method. In principle, any point that can be identified in the first or second derivative of the potential of the formation and the reference can be used. Characteristic points that have been identified and used in this work are marked in Figure 3. Here, triangles depict characteristic points from the first derivative, as shown in Figure 3b, and squares mark features from the second derivative, as shown in Figure 3c. Features of the reference are depicted with blue-filled markers. Features from the formation measurement are shown with red-filled markers. Based on this, the SEI capacity can be calculated for any identified feature according to Equation (7) and (8).

3.2.2. Time Series-Based Method

The SEI capacity is described as equidistant time series, $Q_{\mathrm{SEI},k}^{\mathrm{TS}}$ with k being a time step at the point in time t_k. This can be used to estimate the potential of the formation curve based on the reference measurement. By minimizing the difference between the differential voltage of the potential of the formation measurement and the estimated potential, the SEI capacity loss during formation can be identified. The method is referred to as TS method and is summarized in this section. Technical details are provided in Section S3, Supporting Information.

The time series is used to estimate the continuous capacity loss due to SEI growth, $Q_{\mathrm{SEI}}(t)$. With the continuous SEI capacity curve, the potential during the formation for the respective charging direction is obtained using the reference measurement as

$$\Phi_{\mathrm{ne,est}}^{\mathrm{ch/dch}}(Q^0) = f_{\mathrm{ne,ref}}^{\mathrm{ch/dch}}\left(\frac{Q^0 - Q_{\mathrm{SEI}}}{C_{\mathrm{ne}}^{\mathrm{Ah}}}\right) \text{for } Q^0 \in \Omega_{\mathrm{est}}^{\mathrm{ch/dch}} \tag{13}$$

The estimated potential is only defined for Q^0 within $\Omega_{\mathrm{est}}^{\mathrm{ch/dch}}$, which specifies the capacity space where data of the reference measurement are available.

The derivatives of the estimated, $\widehat{d}_{\mathrm{est},i}^{\mathrm{ch/dch}}$, and measured, $\widehat{d}_{\mathrm{form},i}^{\mathrm{ch/dch}}$, formation potential curve are calculated at equidistant throughput capacities Q_i. For each capacity, Q_i the difference between the formation measurement and the estimated differential potential can be calculated as

$$\widehat{e}_{\mathrm{DV1},i}^{\mathrm{ch/dch}} = \widehat{d}_{\mathrm{form},i}^{\mathrm{ch/dch}} - \widehat{d}_{\mathrm{est},i}^{\mathrm{ch/dch}} \tag{14}$$

in the respective charging direction. In addition, the difference between the capacities at characteristic points with equal potentials at the beginning of the first charge, γ_1, and at the end of the first discharge, γ_2, are calculated. At these points, the slope of the potential is steep, which allows an accurate estimation of the capacity loss and helps to make the optimization process more robust. The errors at these points are given by $e_{Q,1}$ and $e_{Q,2}$, respectively. To identify the time series, the difference between formation and estimation is minimized as

$$\min_{Q_{\mathrm{SEI}}}\left[\sum\left[w_{\mathrm{DV1}}^{\mathrm{ch}}\,\widehat{e}_{\mathrm{DV1},i}^{\mathrm{ch}}\right]^2 + \sum\left[w_{\mathrm{DV1}}^{\mathrm{dch}}\,\widehat{e}_{\mathrm{DV1},i}^{\mathrm{dch}}\right]^2 + \left[w_{Q,1}\,e_{Q,1}\right]^2 \right.$$
$$\left. + \left[w_{Q,2}\,e_{Q,2}\right]^2\right] \tag{15}$$

with w being weighting factors of individual parts of the objective function. The applied weighting factors are listed in Table S3, Supporting Information. The function is minimized using the SEI capacity as an input.

The results of this optimization process are shown in **Figure 4** for the example of cell 1. Results of cells 2–6 are provided in Figure S3–S7, Supporting Information. The experimental and estimated anode potential curves in charge direction and its first derivative are shown in Figure 4a,b, respectively. While the experimentally obtained formation curve is depicted as a dashed gray line, the estimated curve using the TS method is shown as a
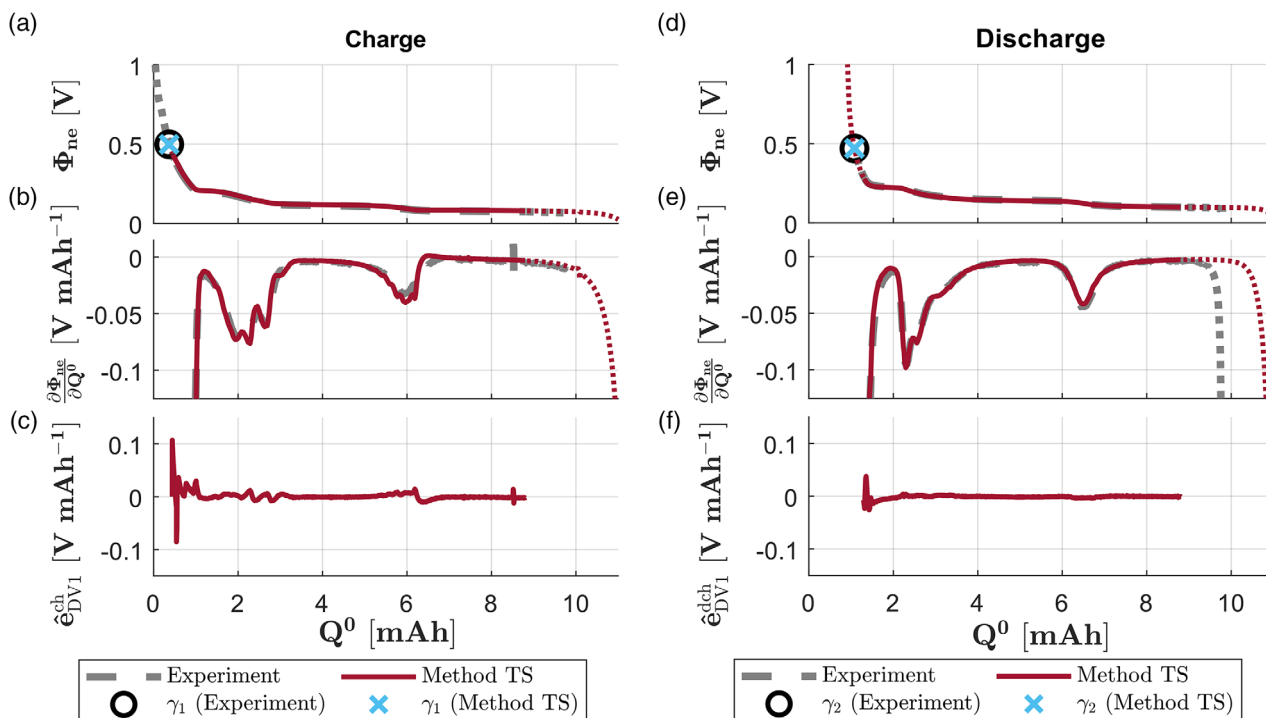

Figure 4. a) Anode potential for charge, b) differential voltage for charge, c) error of the differential voltage for charge, d) anode potential during for discharge, e) differential voltage for discharge, and f) error of the differential voltage for discharge. Dashed gray lines show the formation and solid red lines show the estimation using TS method for cell 1. Section outside of the comparison range is displayed as dotted lines in the respective colors. Characteristic features, γ_1 and γ_2, for the experiment and estimation are highlighted with a black circle (experiment) and a light blue cross (estimation).

**ADVANCED
SCIENCE NEWS**

www.advancedsciencenews.com

Energy Technology
Generation, Conversion, Storage, Distribution

www.entechnol.de

solid red line. Parts of the potential curves that were cropped are shown as dotted lines. The additional features, γ_1, at the beginning of the formation, are marked as a black circle (experiment) and blue cross (estimation). The deviation between the first derivatives of the experimental and estimated formation potential curves is shown in Figure 4c. Similar to the described curves in charge direction, in Figure 4d–f, the anode potential (d), the corresponding first derivative (e), and the deviation of the experimental and estimated differential voltage curves (f) are shown as a function of the capacity during the first discharge.

To evaluate the quality of the identified SEI thickness, solely the deviations between the first derivatives of charge and discharge are used. The error is calculated as

$$e_{\text{curve}} = \sum \sqrt{\hat{e}_{\text{DV1},i}^{\text{ch}}{}^2} + \sum \sqrt{\hat{e}_{\text{DV1},i}^{\text{dch}}{}^2} \tag{16}$$

3.2.3. Growth Model-Based Method

SEI capacity loss can be determined using various SEI growth models. This method is referred to as GM method. The method is similar to the previous one as it also estimates the formation potential with Equation (13) and minimizes Equation (15). The weights used for method GM are also listed in Table S3, Supporting Information. However, instead of adjusting sample points of a time series, the dynamic growth process is described with an ordinary differential equation. Parameters of the models are adjusted during the optimization process. In principle, any empirical or physics-motivated growth model, for example, the models of Colclasure et al.[48] or Kolzenberg et al.,[61] could be tested. Thus, the method allows to directly identify model parameters using the differential voltage.

The models that have been applied in this work assume that the layer growth only depends on the SEI layer thickness and electrical potential at the interphase. Three models have been used: ET, interstitial diffusion (ID), and concurrent (CC) occurrence of both mechanisms. A detailed derivation of the ET and ID mechanisms can be found in the studies of Tang et al.[25] and Single et al.,[62] respectively. ET and ID mechanisms have been chosen, because these were demonstrated to be possible transport mechanisms in the early SEI formation in the first-principle study by Soto et al.[20]

The ET model is given as

$$\frac{\mathrm{d}Q_{\text{SEI,ET}}}{\mathrm{d}t} = A_{\text{ne}}\, i_{0,\text{SEI}}\, \exp\left(-\beta\, L_{\text{SEI}}\right) \exp\left(\frac{-\alpha_{\text{SEI}}\, \mathrm{F}\, \eta_{\text{SEI}}}{\mathrm{R}T}\right) \tag{17}$$

with $i_{0,\text{SEI}}$ being the exchange current density, β being the tunneling barrier, η_{SEI} being the overpotential, α_{SEI} being the symmetry factor, R being ideal gas constant, and T being the temperature. The SEI thickness, L_{SEI}, is derived from the SEI capacity, as given by Equation (11) and (12). The overpotential, η_{SEI}, driving the reduction reaction at the interphase is calculated as

$$\eta_{\text{SEI}} = \Phi_{\text{ne}} - \Phi_{\text{eq,SEI}} \tag{18}$$

with $\Phi_{\text{eq,SEI}}$ being the reaction equilibrium potential, which we assume to be a constant value of 0.8 V, which is commonly chosen in literature.[36,62] Further losses due to ohmic and ionic

resistances are neglected and the potential is assumed to be constant within the electrode, which is justified by the low currents applied during formation. The symmetry factor, α_{SEI}, the tunneling barrier, β, and the exchange current density, $i_{0,\text{SEI}}$, are identified based on the measurement.

The layer growth via diffusion of lithium interstitials is modeled as

$$\frac{\mathrm{d}Q_{\text{SEI,ID}}}{\mathrm{d}t} = A_{\text{ne}}\, \mathrm{F}\, \frac{D_{\text{SEI}}}{L_{\text{SEI}}}\, c_0\, \exp\left(\frac{-\Phi_{\text{ne}}\, \mathrm{F}}{\mathrm{R}\, T}\right) \tag{19}$$

with c_0 being the average lithium concentration in the SEI and D_{SEI} being the diffusion coefficient of the lithium interstitials. To circumvent the undefined state at $L_{\text{SEI}} = 0$, the growth rate is limited to a maximum value, which is defined by means of an assumed minimum limiting layer thickness of 10 pm. The diffusion coefficient D_{SEI} is identified based on the measurement.

We also consider the CC growth via ET and the diffusion of lithium interstitials. The CC mechanism is modeled by the superposition of both growth models.

$$\frac{\mathrm{d}Q_{\text{SEI,CC}}}{\mathrm{d}t} = \frac{\mathrm{d}Q_{\text{SEI,ET}}}{\mathrm{d}t} + \frac{\mathrm{d}Q_{\text{SEI,ID}}}{\mathrm{d}t} \tag{20}$$

Identified parameters are equal to the ID and ET models. All the constants used for the SEI growth models as well as for the conversion of the capacity to the effective SEI thickness are summarized in Table S4, Supporting Information.

An example result for the GM method, with mechanism CC, is shown in **Figure 5** for cell 1. Results of cells 2–6 are provided in Figure S8–S12, Supporting Information. Figure 5a, shows the experimental (dashed gray) and estimated (solid blue) anode potential during the first charge. Figure 5d shows the same in the discharge direction. Anode potential sections that lie outside of the comparison range are shown as dotted lines. The additional characteristic features in the beginning and end of the formation are depicted as a black circle (experiment) and a light blue cross (estimation). Figure 4b,e shows the first derivatives of the experimental and estimated formation potential curves with respect to the capacity in charge and discharge direction, respectively. The corresponding deviation curves between experimental and estimated formation potential curves are shown in Figure 4c,f during the first charge and discharge, respectively.

3.3. Assumptions and Scope of Application

The presented methods for identification of the capacity loss and SEI thickness during formation imply several major assumptions, which are briefly outlined as follows: 1) The impact of side reaction overpotentials during the first cycle on the differential voltage characteristics is negligible. 2) The influence of other aging mechanisms, for example, graphite exfoliation, is assumed to play a minor role due to the high specific surface area.[63] 3) To calculate an effective thickness, the influence of the SEI composition on the average SEI density and morphological aspects can be neglected. As a consequence, the thickness of an effective dense layer is estimated directly using the measured capacity loss. 4) Specific surface area scales linearly with the electrode capacity. 5) Features of the differential voltage are mainly
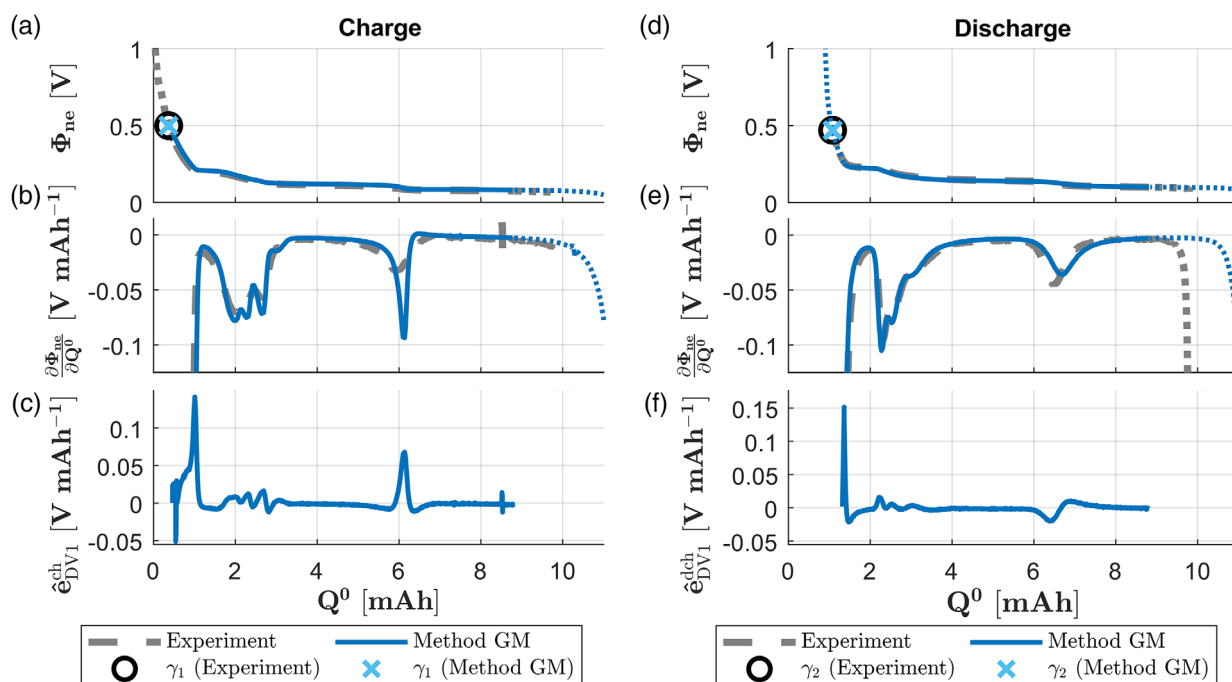
2200688 (7 of 15)

Figure 5. a) Anode potential for charge, b) differential voltage for charge, c) error of the differential voltage for charge, d) anode potential during for discharge, e) differential voltage for discharge, and f) error of the differential voltage for discharge. Dashed gray lines show the formation and solid blue lines show the estimation using GM method with CC model for cell 1. Sections outside of the comparison range are displayed as dotted lines in the respective colors. Characteristic features, γ_1 and γ_2, for the experiment and estimation are highlighted with a black circle (experiment) and a light blue cross (estimation).

determined by the active material and appear at specific degrees of lithiation. As long as the material structure is not compromised, neither the SEI nor the electrolyte composition significantly affects the position of these features.

We emphasize that these assumptions need to be carefully taken into consideration while interpreting the results. We will refer to these assumptions accordingly in our discussion.

The assumptions provided earlier also impact the scope of application of the proposed method. It is well known that some electrolyte solutions can degrade the active material and can lead to active material loss due to graphite exfoliation or particle cracking.[64–66] As outlined earlier, it is assumed that only the side reactions and film growth are influenced by the electrolyte and not the active material. In the case of testing an electrolyte that may damage the active material, the current method does not work reliably. To take these effects into account, further refinement of the method is needed. However, both electrolytes studied here can be expected to form a stable SEI, as they are based on ethylene carbonate (EC) and ethyl methyl carbonate (EMC) solvents. The OCVs after formation are provided in the supporting information and show that the active material features are not significantly affected.

4. Results and Discussion

In this section, the results of the described methods are discussed. First, the methods are compared with respect to their accuracy in terms of their fit quality and physical feasibility.

Second, TS and GM methods are compared with respect to their applicability to investigate the impact of electrolyte additives. Finally, the impact of the chosen SEI growth model and a first physical insight on SEI growth utilizing such growth models are depicted.

4.1. Comparison of the Applied Methods

The shift of the anode potential during formation with respect to the reference was performed using three methods. Although SP method was performed manually, TS method and GM each are solved using the objective function in Equation (15). Here, the CC model is considered for the model-based method.

The SEI growth as determined for cell 1 using the three methods is shown in **Figure 6**. The methods are indicated with different colors and markers: yellow triangles for SP method, red circles for TS method, and solid blue line for GM–CC method. Independent of the method, a general growth trend can be seen. The SEI thickness rises rapidly in the early part of the first charge. After reaching an effective layer thickness of ≈1.9 nm the growth rate slows down and ends at the same layer thickness of ≈3.5 nm for all methods. While the first part and final thickness is almost congruent for all methods, the growth curves in between differ. The GM–CC method-based effective layer thickness increases continuously. After the initial rapid build-up, the growth rate slows down at first but temporarily accelerates again in low-anode-potential regions in the time range 15 − 22 h during charge. At the end of the charge step, the majority of the SEI
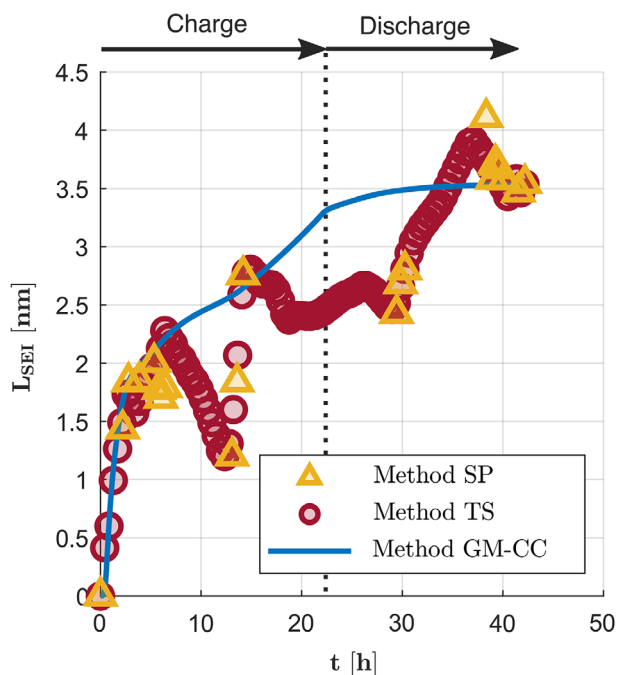
ADVANCED
SCIENCE NEWS
www.advancedsciencenews.com

Energy Technology
Generation, Conversion, Storage, Distribution

www.entechnol.de

Figure 6. SEI thickness as a function of the formation time obtained by the three methods, that is, SP, TS, and GM methods, for cell 1. The layer thickness at the feature points based on SP method is marked with yellow triangles. The growth estimation using TS method is displayed with red circles. The continuous growth estimation calculated with GM method and mechanism CC is plotted with a solid blue line.

is already built. During discharge, the growth rate further decreases. This asymmetric growth depending on the charge direction was also reported by Attia et al.[67] In comparison, the growth curves of SP and TS methods differ. The main difference is that both show negative growth temporarily. The negative growth is physically not plausible, because it indicates recovery of charge carriers. This should not be possible, because the SEI reaction is irreversible. The GM methods prevent negative growth due to appropriate model assumptions. In contrast, SP and TS methods are not restricted by physical assumptions. For the TS method, this is utilized to further minimize the objective function by compressing the capacity curve in flat potential areas. Comparing TS and SP methods, it can be seen that almost all features identified by the SP method lie within the curve obtained using the TS method.

The deviation between the experimental formation and estimated formation is assessed using Equation (16) and shown in **Figure 7**a for TS and GM methods for all investigated cells. Concerning cell 1, it can be seen that the error of the GM–CC method is more than twice as large as the error of TS method. The detailed results of this cell are depicted in Figure 4 and 5. It can be seen that for both methods the curves for the anode potential and the differential voltage are in good agreement. In Figure 5b, it can be seen that for the GM–CC method, the features of the experiment and the estimation occur at approximately the same capacities, for example, at 6 mAh during charge, which indicates that the growth rate is depicted accurately. In Figure 4b, it can be seen that the derivative matches even better for TS method, because the curve better adapts to the shape of the feature. This can also be seen in the deviation between the experimental and estimated curves depicted in Figure 4c and 5c,
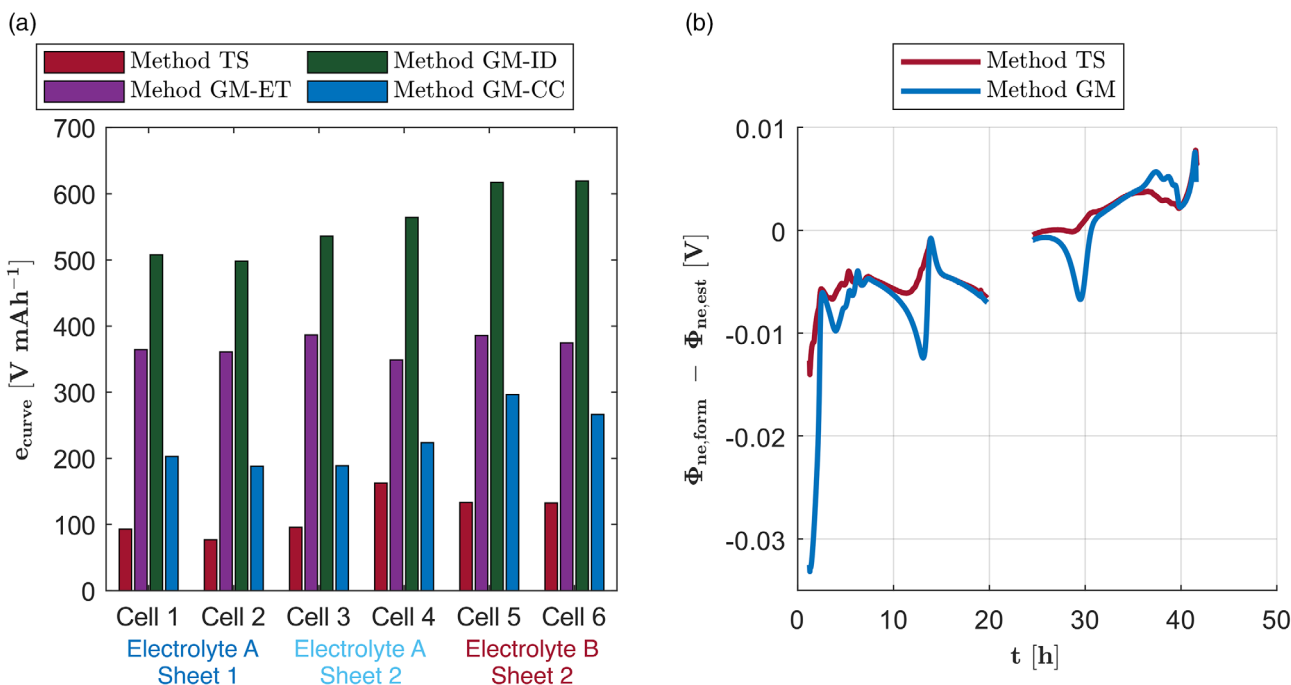

Figure 7. a) Deviation between the experimental and estimated formation curve for TS and GM methods for each cell. The error of TS method is shown in red. The error of GM method using different models are depicted in purple (ET), green (ID), and blue (CC). b) Deviation between the experimental and estimation of the formation anode potential curve of cell 1 for TS method (red) and GM–CC (blue).

**ADVANCED
SCIENCE NEWS**
www.advancedsciencenews.com

Energy Technology
Generation, Conversion, Storage, Distribution

www.entechnol.de

respectively. While the deviation for TS method at the features shows very short spikes, the error is high over longer ranges around the features with also greater magnitudes for the GM–CC method. In Figure 4d and 5d, the corresponding discharge curves are shown. For both methods, the experimental and estimated curves are again in good agreement for discharge, as shown in Figure 4e,f and 5e,f. Differences between the two methods can be seen at the first-stage transition during discharge ($Q^0 \approx 6.5\,\text{mAh}$). In particular, the first peak of the estimated formation curve for the GM–CC method appears at a higher Q^0 of $\approx 6.68\,\text{mAh}$. The minimum of the differential voltage in the experiment is at $Q^0 \approx 6.5\,\text{mAh}$. This indicates an overestimation of SEI capacity at this position using the GM–CC method. To conclude, the increased error for the GM method in comparison with the TS method is mainly due to a higher divergence occurring in certain areas, but it might also indicate that the applied model is not fully consistent with the experiment and further refinement is needed.

Further differences can be seen in Figure 7b, which show the deviation between the formation potential curves and the estimated curves. The difference using TS method is given as a red line. The difference using the GM–CC method is given as a blue line. It can be seen that the deviations are located around the stage transitions and are more pronounced for the GM–CC method. This confirms that the better fit quality of the TS method can be attributed to its higher degree of freedom, which especially allows to minimize the deviation around stage transitions.

In general, a difference between the estimated potential and the actual formation, as shown in Figure 7b, can be expected due to the mixed potential of the electrode and the additional electrode polarization caused by the SEI formation reaction, which may also change during formation as the side reaction is not completed. Nevertheless, it can be seen that the average potential difference is bigger during charge than during discharge for both methods. This also implies that the voltage loss due to the SEI formation side reactions decreases as the formation progresses. This observed parallel shift of the electrode potential challenges assumption 1 reported in Section 3.3, which states that the reaction overpotential during the first cycle is negligible.

To sum up, all applied methods show similar trends for the effective SEI thickness. It increases rapidly in the beginning of the first charge and growth more slowly later in the first discharge. TS and SP methods show negative SEI growth, which is not physically plausible. GM method does not possess negative growth rates due to physical assumptions but shows larger errors for the differential voltage. Results indicate that TS method can better adapt to distorted slopes of the differential voltage at stage transitions, which reduces the error, but might lead to artifacts for the estimated effective SEI thickness.

4.2. Comparison of the SEI Growth for a Variation of Electrolytes

The TS and GM methods have been applied to investigate the influence of two different electrolyte compositions. The measurements with electrolyte A were conducted using two different
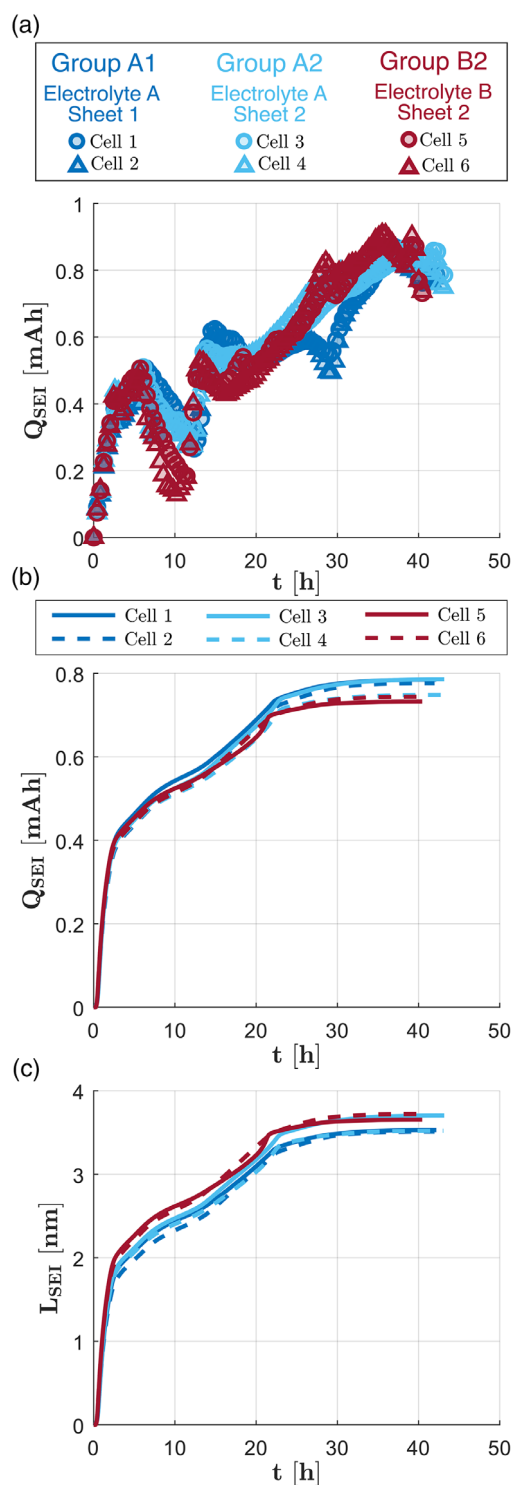

Figure 8. a) SEI capacity as a function of time obtained with TS method. Cell groups are shown in blue (group A1, cells 1–2), light blue (group A2, cells 3–4), and red (group B2, cells 5–6). First and second cells of each group are marked with circles or triangles in the respective group color. b) SEI capacity as a function of time obtained with GM–CC method. First and second cells of each group are plotted as a solid or dashed line in the color of the respective group. c) SEI thickness as function of time corresponding to the capacitance curve determined with GM–CC method.

electrode sheets to assess the possible influence of production variances. Electrolyte B was only tested with cells built from sheet 2.

The obtained SEI capacity and effective thickness curves using TS method and GM–CC are shown in **Figure 8**. Figure 8a shows the resulting SEI capacity curves determined with TS method as a function of time for all investigated cells. It can be seen that for all cells the SEI grows quickly in the beginning and slows down afterward. Within a cell group, there are only minor deviations between the capacity trends. Moreover, the capacity curve of the cells containing electrolyte A (group A1 and A2, cells 1–4) is nearly congruent during charge. During discharge, cells 1 and 2 show a kink at about 30 h, which cannot be seen for cells 3 and 4, even though the same electrolyte was used. Minor differences are observable between two electrolytes at the beginning of the formation. In comparison with electrolyte A, more capacity is bound during the early formation phase for cells 5 and 6, built with electrolyte B. After reaching an SEI capacity of $Q_{SEI} \approx 0.42$ mAh, the capacity drops for all cells. This decline is more pronounced for electrolyte B. All cells then quickly return to their previous SEI capacity. Thereafter, the cells built from sheet 2 proceed similarly and only small differences are noticeable. The capacity increases slightly faster with electrolyte B. The capacity of cells from group A2 (cells 3 and 4) grows almost linearly. At $t = 30$ h, a kink can be observed for cells 5 and 6. However, the kink is reversed in comparison with group A1. At the end of the formation, the SEI capacity decreases slightly again. This is most pronounced for cells of group B2. The general trend of the SEI capacity curve can be identified and is similar for all cells. However, due to the kinks of the curves, being presumably artifacts of the TS method, it is difficult to identify significant and meaningful differences between the cells.

The SEI capacity curves obtained by the GM–CC method are depicted in Figure 8b for all cell configurations. In the beginning of charging, that is, $0 - 0.5$ h, the SEI capacity rises steeply for all cells. This steep SEI capacity increase continues until an SEI capacity Q_{SEI} of ≈ 0.4 mAh is reached. Thereafter, the capacity rise slows down at first and accelerates again from $t \approx 15$ h until the end of the first charge. At the end of the first charge, the SEI capacities differ slightly. Cells built with electrolyte A reach SEI capacity between $Q_{SEI} \approx 0.71$ mAh and $Q_{SEI} \approx 0.735$ mAh. For cell 5 and 6, ≈ 0.695 and ≈ 0.69 mAh was bound in the SEI during the first charge, respectively. During discharge, the capacity rise continuously slows down. At the end of the first cycle, the cells are lost between 0.73 and 0.785 mAh. In general, it seems that capacity loss is lower for electrolyte B. In comparison with TS method, the capacity curves do not possess artifacts, which allow to differentiate the capacity curves. However, the differences between the investigated cells are insignificant given the capacity differences of the electrodes.

The SEI capacities have been used to calculate the effective layer thickness using Equation (12). The effective layer thicknesses determined by means of the GM–CC method are shown in Figure 8c. Due to assumed linear connection between the capacity losses and the effective SEI thickness, the overall course of the layer growth is essentially the same. Nevertheless, by converting the capacity into an effective thickness, which takes the individual electrode capacity into account, differences for the SEI

growth between the electrolytes can be seen. As previously described for the capacity curves, SEI grows rapidly for all cells initially. After an effective thickness of ≈ 1.85 nm has been reached, the growth rate decreases for electrolyte A. For cells with electrolyte B, the steep growth continues up to an effective layer thickness L_{SEI} of ≈ 2 nm before the growth rate also slows down. Subsequently, the effective layer thicknesses with electrolyte B are above those of electrolyte A throughout the remaining charging process. As in the capacity curve, the growth of the layer accelerates toward the end of the first charge. This growth is particularly pronounced for cell 4. For the other cells, the effective thickness accelerates similarly. In contrast to the capacity curve, the effective layer thicknesses seem to converge during the discharge process. By taking into account the cell individual electrode capacity, all cells have a similar effective layer thickness L_{SEI} at the end of the formation, ranging from ≈ 3.51 to ≈ 3.72 nm. This suggests that the final SEI thickness is not influenced by the electrolyte, even though the build-up process seems to be different.

However, when comparing different electrolytes with this method the error needs to be considered. In Figure 7a, it can be seen that the error of the GM–CC method for cells 5 and 6 using electrolyte B is considerably larger compared with cells 1–4 using electrolyte A. In this context, other possible causes that may influence the DVA curves during the formation, for example, different side reaction overpotentials or SEI properties, must be carefully considered. Both causes cannot be completely ruled out with the currently available data and may distort the DVA curves. Further studies are needed to assess their impact. However, in comparison with the potential changes due to the stage transitions, the impact of electrolyte-dependent changes in overpotentials due to the side reactions or SEI properties is minimal since the features were clearly identifiable for all cells.

To sum up, even so in this example, only minor differences between the electrolytes could be revealed, the method seems to be appropriate to quickly obtain an estimate of the SEI layer growth during formation, which allows to study a large number of influencing factors with minor experimental effort.

4.3. Comparison of the Applied SEI Growth Models

The GM method can be used to parameterize and validate SEI growth models. The estimated growth curves for the three mechanisms (ET, ID, and CC) are shown in **Figure 9**. The results of the ET model are plotted in purple (GM–ET). It can be seen that for GM–ET the SEI growth is initially very steep. At an effective layer thickness of ≈ 2.1 nm the growth continuously slows down and reaches a final effective SEI thickness of ≈ 3.05 nm. At the end of the formation, the SEI growth is almost flat. The results for the ID model are depicted in green (GM–ID). The SEI growth significantly differs from the ET model. SEI growth is very slow at first and then increases until an effective layer thickness of ≈ 3.05 nm is reached during the first charge. The growth rate significantly slows down during discharge. The final effective SEI thickness is ≈ 3.53 nm. GM–CC method, the combination of both mechanisms, is shown in blue. The curve with the CC model has been described in Section 4.1. In the beginning
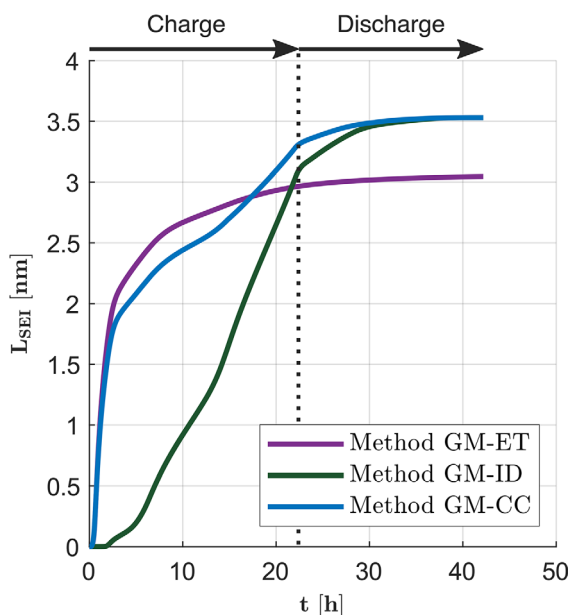
ADVANCED
SCIENCE NEWS
www.advancedsciencenews.com

Energy Technology
Generation, Conversion, Storage, Distribution
www.entechnol.de

Figure 9. SEI thickness as a function of the formation time obtained with different growth models using the GM method. GM–ET (purple) indicates the results for the GM method using the ET model. GM–ID (green) indicates the results for the GM method using the ID model. GM–CC (blue) indicates the results for the GM method using the CC model.

(until $t \approx 15\,$h) it follows the trend of the ET model, whereas later it is rather dominated by the ID model.

The models also posses different errors. The errors using the different growth mechanisms are shown in Figure 7 for all cells. GM–ID is plotted in green and shows the largest total error for every cell. The reason is that the mechanism ID does not depict the strong growth at the beginning of the formation. The error of the ET model is shown in purple. In comparison with the ID model, it shows reduced errors. This is mainly because the ET model can accurately depict the initial steep SEI growth. Nevertheless, ET model does show a larger error compared with the CC model for all cells. As the ET model and the CC model show a very similar slope in the beginning, the larger error of the ET model is caused at the later phase of the formation. The error of the CC model is displayed in blue and is the lowest of the investigated growth mechanisms for all cells. The CC ET and diffusion of interstitials explain the steep initial growth as well as the layer growth after the effective SEI thickness evolved beyond the ET regime. This is discussed in more detail in the following section.

To sum up, the study demonstrates that with this method various models can be compared and evaluated with respect to their error of the differential voltage. The CC model has the lowest error of the investigated models and therefore is superior compared with the other models. Nevertheless, the error is still significant. At this stage, it cannot be finally concluded if this deviation is due to an insufficient model or due to the uncertainty of the introduced DVA-based method. Possible factors of uncertainty were discussed in the previous Section 4.2. Yet, the results suggest that the SEI growth during

the first cycle of the formation can be explained by a combination of ET and ID but not solely by one of the mechanisms.

4.4. Application to Quantify the Impact of Electrolytes

To gain further insights into the SEI growth mechanisms, results of the GM–CC method are shown and discussed in more detail. The contribution of the transport mechanisms to the total growth is given as a function of time for cell 1 in **Figure 10**. The CC model combines the ET and ID mechanisms, as given in Equation (20). The relative contribution of the ET term to total growth within the CC model is shown in purple. The share of the ID term within the CC model is shown in green. At the beginning of the formation, ET is unity. This was reported before for a situation where the reactant and electrode were in close or direct contact.[25] After $\approx 4\,$h the share of ET reduces. Subsequently, the share of the ET mechanism decreases with time and effective layer thickness. At the same time, the contribution to the overall growth rate due to ID mechanism increases. At $\approx 9.6\,$h both transport mechanisms contribute equally, that is, 0.5, to the growth. This point in the formation time is labeled as $t_{SEI,0.5}$. Afterward, the ID mechanism is the main contributor to the overall SEI growth. Only at the end of the formation, in higher-potential regions, ET adds to the growth again. However, we note that in this region the overall growth rate is very low. The proportional progression of transport mechanisms is similar for all cells regardless of the used electrolyte. Yet, differences between the electrolytes can be seen by comparing the identified parameters of the growth model as well as for the effective layer thickness $d_{SEI,0.5}$, which depicts the effective layer thickness at $t_{SEI,0.5}$. It indicates the transition point between ET and ID mechanisms.

The parameters and $d_{SEI,0.5}$ are summarized in **Table 1**. The ET barrier β and the diffusion coefficient of the lithium interstitials D_{SEI} do not show clear differences between the cells.
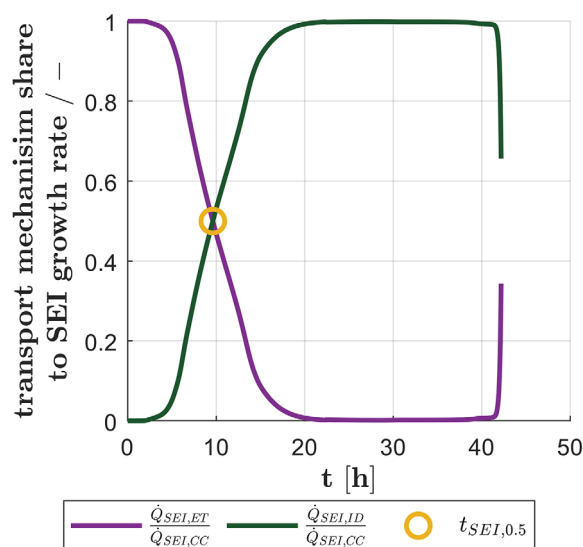

Figure 10. Relative contribution of the ET mechanism (purple) and ID mechanism (green) to the overall growth rate of the CC model as a function of the formation time for cell 1.

ADVANCED
SCIENCE NEWS
www.advancedsciencenews.com

Energy Technology
Generation, Conversion, Storage, Distribution
www.entechnol.de

Table 1. Fitted parameters of GM-CC method for all cells.

Group	Cell no.	$d_{SEI,0.5}$ [nm]	$i_{0,SEI}$ [A m^{-2}]	α_{SEI} [−]	β [nm^{-1}]	D_{SEI} [m^2 s^{-1}]
Electrolyte A	Cell 1	2.42	224.35×10^{-6}	0.539	6.68	4.565×10^{-15}
Sheet 1	Cell 2	2.28	263.82×10^{-6}	0.495	6.6	5.105×10^{-15}
Electrolyte A	Cell 3	2.45	251.59×10^{-6}	0.541	6.66	4.683×10^{-15}
Sheet 2	Cell 4	2.45	279.91×10^{-6}	0.525	6.66	3.293×10^{-15}
Electrolyte B	Cell 5	2.66	301.79×10^{-6}	0.559	6.49	3.426×10^{-15}
Sheet 2	Cell 6	2.53	385.96×10^{-6}	0.553	6.72	5.235×10^{-15}

However, the cell groups can be differentiated by the exchange current density $i_{0,SEI}$, the symmetry factor α_{SEI}, and the transition point of the mechanisms $d_{SEI,0.5}$. The determined model parameters, α_{SEI} and $i_{0,SEI}$, indicate differences between the electrolytes and show the same trend. Both are bigger for the cells built with electrolyte B (group B2). For electrolyte A, both model parameters are lower overall, regardless of the electrode sheet. Although the difference for the symmetry factor α_{SEI} is small, the trend is more pronounced for the exchange current density $i_{0,SEI}$. With respect to the two model parameters, no clear tendency is discernible between groups A1 and A2. For the transition points of the mechanisms, $d_{SEI,0.5}$, small differences between the groups and also between the electrolytes are noticeable. Overall $d_{SEI,0.5}$ is between 2.42 and 2.66 nm, which is in line with previously reported typical ET length for inorganic species.[39] It is smallest for group A1, followed by group A2, and highest for cells with electrolyte B (group B2). The cells using electrolyte A (groups A1 and A2), with the exception of cell 2, show minor deviations. Even though the deviations are small overall, this indicates that the results are disturbed by manufacturing uncertainties and underline that the cell individual surface area is an important input parameter. Despite the uncertainties, the cells built with electrolyte A can be clearly separated from the cells built with electrolyte B regardless of the electrode sheet. This indicates an influence of the electrolyte on the SEI growth mechanism, which can be quantified using the presented method.

5. Conclusion

In this work, a novel method to investigate SEI growth has been presented. This method is based on DVA and coulomb counting. In general, features of the differential voltage of the formation are identified and compared with a reference measurement. As shown in this article, this can be used to estimate the capacity loss due to the SEI growth during the initial cycle of the formation process. Further, using the SEI density and the surface area of the electrodes, a cell individual effective SEI thickness has been calculated.

Three different methods have been introduced and applied to deduce SEI growth curves. First, single-characteristic points were used. Second, a time series of equidistant capacities was fit to the continuous experimental formation curve. Third, a continuous SEI growth curve was obtained using growth models, which comprised ET, ID, and the CC combination of both as possible

transport mechanisms. Analysis of single-characteristic points and the time series approach showed similar results. The time series approach showed the lowest error, but showed partially negative SEI growth, which is physically not plausible. The growth model-based approach showed larger errors but was physically plausible.

Regardless of the particular method, a general growth trend has been observed. The obtained SEI capacity curves rise steeply at the beginning of the first charge. In the further course of the charging process, the growth slows down at first but accelerates again in low-potential ranges before the growth rate continuously decreases during discharge.

With the model-based approach, it has been shown how the method can be used to review and parameterize SEI growth models. In this study, the CC combination of ET and ID (CC model) showed the lowest error. Solely ET or ID does not explain the entire SEI growth during the first cycle of the formation.

Furthermore, differences between electrolytes or electrode sheets for cell formation could be revealed with low experimental effort. We note that these differences are not always significant and need to be considered in the context of the assumptions of the method. The analysis of the SEI layer thickness is sensitive to the assumed surface area of the electrode. In this work, the surface area has been estimated based on cell individual electrode capacities, which introduce uncertainty in the quantitative analysis of the layer thickness. The neglect of the side reaction overvoltage and SEI properties, which both change during formation and might be influenced by the electrolyte, adds another uncertainty. These need to be considered carefully when comparing different electrolytes. Nevertheless, the current results indicate that different electrolytes shift the effective layer thickness in which ET is dominant. This suggests a difference in the composition or structure of the SEI, which needs to be validated experimentally in future investigations.

Future work should address various challenges associated with this method. This includes an improvement regarding the estimation of the electrode surface area. For comparison of electrolytes, the validity of assumption 5, that is, that the position of graphite stage transitions is not affected by the electrolyte, must be considered carefully. Some electrolytes might cause damage to the active material structure, which would compromise this assumption. Further, the observed negative SEI growth needs to be analyzed in more detail to reveal the underlying causes. The method should be tested with further application examples, which should possess a larger number of samples.

2200688 (13 of 15)

**ADVANCED
SCIENCE NEWS**
www.advancedsciencenews.com

Energy Technology
Generation, Conversion, Storage, Distribution
www.entechnol.de

Additional measurements are also needed to improve the robustness of the algorithm. So far, it has proven intricate to identify a set of weighting factors working equally well for all cells. Further, the DVA-based results should be compared with other complementary experimental methods. This will improve the method, its validity, and reliability.

To conclude, the developed method provides operando information on the SEI formation during the first cycle with low experimental effort. This can be utilized in several promising future applications. The method is in principle also applicable to full-cell voltage as was shown by Bloom et al.[68] in their aging study. This allows its application within battery cell production lines for cell quality assessment and potentially provides useful characteristics about aging already during the formation process. The importance of using early data for predicting capacity degradation was already pointed out by Severson et al.[69] and can potentially be addressed with this method in the future. As the method allows to characterize essential aspects of the SEI layer growth, it is suitable for the analysis of factors influencing the SEI growth, for example, for the screening of electrolytes. This is a promising approach to accelerate development processes and thus reduce development costs. In addition, the method can be used to identify and parameterize SEI growth models. This may provide information on the influence of the formation protocol onto SEI and yield insights into growth mechanisms. Finally, these parameterized growth models can be used to simulate and optimize formation protocols.

Supporting Information

Supporting Information is available from the Wiley Online Library or from the author.

Acknowledgements

Conflict of Interest

The authors declare no conflict of interest.

Data Availability Statement

The data that support the findings of this study are available from the corresponding author upon reasonable request.

Keywords

[1] M. Winter, *J. Phys. Chem. C* **2009**, *223*, 1395.
[2] P. Verma, P. Maire, P. Novák, *Electrochim. Acta* **2010**, *55*, 6332.
[3] S. Menkin, D. Golodnitsky, E. Peled, *Electrochem. Commun.* **2009**, *11*, 1789.
[4] U. S. Meda, L. Lal, S. M. P. Garg, *J. Energy Storage* **2022**, *47*, 103564.
[5] Y. Yamada, Y. Iriyama, T. Abe, Z. Ogumi, *Langmuir* **2009**, *25*, 12766.
[6] M.-S. Zheng, Q.-F. Dong, H.-Q. Cai, M.-G. Jin, Z.-G. Lin, S.-G. Sun, *J. Electrochem. Soc.* **2005**, *152*, A2207.
[7] G. Park, H. Nakamura, Y. Lee, M. Yoshio, *J. Power Sources* **2009**, *189*, 602.
[8] R. Fong, U. von Sacken, J. R. Dahn, *J. Electrochem. Soc.* **1990**, *137*, 2009.
[9] O. Matsuoka, A. Hiwara, T. Omi, M. Toriida, T. Hayashi, C. Tanaka, Y. Saito, T. Ishida, H. Tan, S. S. Ono, S. Yamamoto, *J. Power Sources* **2002**, *108*, 128.
[10] H. Q. Pham, G. J. Chung, J. Han, E.-H. Hwang, Y.-G. Kwon, S.-W. Song, *J. Chem. Phys.* **2020**, *152*, 094709.
[11] M. E. Spahr, H. Buqa, A. Würsig, D. Goers, L. Hardwick, P. Novák, F. Krumeich, J. Dentzer, C. Vix-Guterl, *J. Power Sources* **2006**, *153*, 300.
[12] S. J. An, J. Li, C. Daniel, D. Mohanty, S. Nagpure, D. L. Wood, *Carbon* **2016**, *105*, 52.
[13] F. Joho, B. Rykart, A. Blome, P. Novák, H. Wilhelm, M. E. Spahr, *J. Power Sources* **2001**, *97–98*, 78.
[14] Y.-B. He, Z.-Y. Tang, Q.-S. Song, H. Xie, Y.-G. Liu, Q. Xu, *J. Electrochem. Soc.* **2008**, *155*, A481.
[15] C. Huang, K. Huang, H. Wang, S. Liu, Y. Zeng, *J. Solid State Electrochem.* **2011**, *15*, 1987.
[16] S. Bhattacharya, A. R. Riahi, A. T. Alpas, *Carbon* **2014**, *67*, 592.
[17] S. Bhattacharya, A. T. Alpas, *Carbon* **2012**, *50*, 5359.
[18] V. A. Agubra, J. W. Fergus, R. Fu, S.-Y. Choe, *Electrochim. Acta* **2014**, *149*, 1.
[19] T. Zhu, Q. Hu, G. Yan, J. Wang, Z. Wang, H. Guo, X. Li, W. Peng, *Energy Technol.* **2019**, *7*, 1900273.
[20] F. A. Soto, Y. Ma, J. M. La Martinez de Hoz, J. M. Seminario, P. B. Balbuena, *Chem. Mater.* **2015**, *27*, 7990.
[21] L. Benitez, J. M. Seminario, *J. Electrochem. Soc.* **2017**, *164*, E3159.
[22] F. Single, B. Horstmann, A. Latz, *J. Electrochem. Soc.* **2017**, *164*, E3132.
[23] E. Peled, *J. Electrochem. Soc.* **1979**, *126*, 2047.
[24] M. Broussely, S. Herreyre, P. Biensan, P. Kasztejna, K. Nechev, R. Staniewicz, *J. Power Sources* **2001**, *97–98*, 13.
[25] M. Tang, K. Miyazaki, T. Abe, J. Newman, *J. Electrochem. Soc.* **2012**, *159*, A634.
[26] C. Hou, J. Han, P. Liu, C. Yang, G. Huang, T. Fujita, A. Hirata, M. Chen, *Adv. Energy Mater.* **2019**, *9*, 1902675.
[27] S. Shi, P. Lu, Z. Liu, Y. Qi, L. G. Hector, H. Li, S. J. Harris, *J. Am. Chem. Soc.* **2012**, *134*, 15476.
[28] H. J. Ploehn, P. Ramadass, R. E. White, *J. Electrochem. Soc.* **2004**, *151*, A456.
[29] M. B. Pinson, M. Z. Bazant, *J. Electrochem. Soc.* **2013**, *160*, A243.
[30] P. Lu, C. Li, E. W. Schneider, S. J. Harris, *J. Phys. Chem. C* **2014**, *118*, 896.
[31] S. Leroy, F. Blanchard, R. Dedryvère, H. Martinez, B. Carré, D. Lemordant, D. Gonbeau, *Surf. Interface Anal.* **2005**, *37*, 773.
[32] D. Witt, F. Röder, U. Krewer, *Batteries Supercaps* **2022**, *5*, e202200067.
[33] J. Lei, L. Li, R. Kostecki, R. Muller, F. McLarnon, *J. Electrochem. Soc.* **2005**, *152*, A774.

[34] M. Nie, D. P. Abraham, D. M. Seo, Y. Chen, A. Bose, B. L. Lucht, *J. Phys. Chem. C* **2013**, *117*, 25381.

[35] P. Niehoff, S. Passerini, M. Winter, *Langmuir* **2013**, *29*, 5806.

[36] K. Edström, M. Herstedt, D. P. Abraham, *J. Power Sources* **2006**, *153*, 380.

[37] T. Yoshida, M. Takahashi, S. Morikawa, C. Ihara, H. Katsukawa, T. Shiratsuchi, J.-I. Yamaki, *J. Electrochem. Soc.* **2006**, *153*, A576.

[38] Y. C. Chen, C. Y. Ouyang, L. J. Song, Z. L. Sun, *J. Phys. Chem. C* **2011**, *115*, 7044.

[39] Y.-X. Lin, Z. Liu, K. Leung, L.-Q. Chen, P. Lu, Y. Qi, *J. Power Sources* **2016**, *309*, 221.

[40] S. Shi, Y. Qi, H. Li, L. G. Hector, *J. Phys. Chem. C* **2013**, *117*, 8579.

[41] Y. Wang, S. Nakamura, M. Ue, P. B. Balbuena, *J. Am. Chem. Soc.* **2001**, *123*, 11708.

[42] C. Wang, A. Appleby, F. E. Little, *J. Electroanalyt. Chem.* **2002**, *519*, 9.

[43] R. N. Methekar, P. W. C. Northrop, K. Chen, R. D. Braatz, V. R. Subramanian, *J. Electrochem. Soc.* **2011**, *158*, A363.

[44] F. Röder, R. D. Braatz, U. Krewer, *J. Electrochem. Soc.* **2017**, *164*, E3335.

[45] F. Röder, V. Laue, U. Krewer, *Batteries Supercaps* **2019**, *2*, 248.

[46] S. Das, P. M. Attia, W. C. Chueh, M. Z. Bazant, *J. Electrochem. Soc.* **2019**, *166*, E107.

[47] J. Christensen, J. Newman, *J. Electrochem. Soc.* **2004**, *151*, A1977.

[48] A. M. Colclasure, K. A. Smith, R. J. Kee, *Electrochim. Acta* **2011**, *58*, 33.

[49] M. Safari, C. Delacourt, *J. Electrochem. Soc.* **2011**, *158*, A1123.

[50] P. Keil, A. Jossen, *J. Electrochem. Soc.* **2017**, *164*, A6066.

[51] S. Schindler, M. A. Danzer, *J. Power Sources* **2017**, *343*, 226.

[52] I. Bloom, J. P. Christophersen, D. P. Abraham, K. L. Gering, *J. Power Sources* **2006**, *157*, 537.

[53] I. Bloom, L. K. Walker, J. K. Basco, D. P. Abraham, J. P. Christophersen, C. D. Ho, *J. Power Sources* **2010**, *195*, 877.

[54] J. P. Fath, D. Dragicevic, L. Bittel, A. Nuhic, J. Sieg, S. Hahn, L. Alsheimer, B. Spier, T. Wetzel, *J. Energy Storage* **2019**, *25*, 100813.

[55] H. M. Dahn, A. J. Smith, J. C. Burns, D. A. Stevens, J. R. Dahn, *J. Electrochem. Soc.* **2012**, *159*, A1405.

[56] V. Müller, R. Kaiser, S. Poller, D. Sauerteig, *J. Energy Storage* **2018**, *15*, 256.

[57] M. Heß, P. Novák, *Electrochim. Acta* **2013**, *106*, 149.

[58] P. Lu, S. J. Harris, *Electrochem. Commun.* **2011**, *13*, 1035.

[59] Y. Zhang, Q. Tang, Y. Zhang, J. Wang, U. Stimming, A. A. Lee, *Nat. Commun.* **2020**, *11*, 1706.

[60] Y. Xie, J. Li, C. Yuan, *J. Power Sources* **2014**, *248*, 172.

[61] L. von Kolzenberg, A. Latz, B. Horstmann, *ChemSusChem* **2020**, *13*, 3901.

[62] F. Single, A. Latz, B. Horstmann, *ChemSusChem* **2018**, *11*, 1950.

[63] S. H. Ng, C. Vix-Guterl, P. Bernardo, N. Tran, J. Ufheil, H. Buqa, J. Dentzer, R. Gadiou, M. E. Spahr, D. Goers, P. Novák, *Carbon* **2009**, *47*, 705.

[64] D. Aurbach, Y. Ein-Eli, O. Chusid, Y. Carmeli, M. Babai, H. Yamin, *J. Electrochem. Soc.* **1994**, *141*, 603.

[65] D. Aurbach, Y. Ein-Eli, *J. Electrochem. Soc.* **1995**, *142*, 1746.

[66] D. Aurbach, A. Zaban, Y. Ein-Eli, I. Weissman, O. Chusid, B. Markovsky, M. Levi, E. Levi, A. Schechter, E. Granot, *J. Power Sources* **1997**, *68*, 91.

[67] P. M. Attia, S. Das, S. J. Harris, M. Z. Bazant, W. C. Chueh, *J. Electrochem. Soc.* **2019**, *166*, E97.

[68] I. Bloom, J. Christophersen, K. Gering, *J. Power Sources* **2005**, *139*, 304.

[69] K. A. Severson, P. M. Attia, N. Jin, N. Perkins, B. Jiang, Z. Yang, M. H. Chen, M. Aykol, P. K. Herring, D. Fraggedakis, M. Z. Bazant, S. J. Harris, W. C. Chueh, R. D. Braatz, *Nat. Energy* **2019**, *4*, 383.